Materials Horizons

ROYAL SOCIETY OF CHEMISTRY

COMMUNICATION

View Article Online
View Journal

Cite this: DOI: 10.1039/d5mh01354b

Received 16th July 2025,
Accepted 11th August 2025

DOI: 10.1039/d5mh01354b

rsc.li/materials-horizons

Ultrathin $WO_3 \cdot H_2O$ nanosheets derived from the Aurivillius phase for high-performance dual-band electrochromic smart windows

Sensen Jia,[a] Xiaodan Guo,[a] Ying Lv,[a] Hang Zhou,[a] Jinhui Wang, *[a] Guojian Yang*[b] and Guofa Cai *[a]

The performance of electrochromic materials is determined by the ion and electron transport. The ion diffusion within active materials generally represents a fundamental limitation for improving electrochromic performance. To enable efficient ion diffusion and ion insertion/extraction, reducing the size and thickness of the active materials is highly desirable. Herein, we report a facile top-down approach for efficiently producing ultrathin $WO_3 \cdot H_2O$ nanosheets *via* ion etching of Aurivillius phase Bi_2WO_6 and liquid-phase exfoliation. Thanks to the ultrathin nanosheet with a thickness of ~4.5 nm, the $WO_3 \cdot H_2O$ film achieves excellent dual-band modulation of 90% at 633 nm and 90.5% at 1200 nm, fast switching within 10 s, and remarkable cycling stability of 5000 cycles. *In situ* measurements disclose that reversible valence change and negligible structural strain of ultrathin nanosheets enable stable electrochromism of $WO_3 \cdot H_2O$. Furthermore, self-powered and large-scale smart windows are demonstrated using the $WO_3 \cdot H_2O$ film and Al foil, realizing a remarkable temperature modulation of 12 °C in a house model. The simulation results reveal that the smart window can reduce the energy consumption of buildings by up to 20.7% (168.8 MJ m^{-2}), demonstrating its excellent thermal regulation and energy-saving capabilities. This ultrathin nanosheet fabrication approach breaks through the inherent inaccessibility of ions within active materials, shedding new light on the exploration of next-generation high-performance electrochromic materials and devices.

New concepts

To address the challenge of achieving efficient ion diffusion and ion insertion/extraction in the electrochromic process, this work introduces an innovative top-down strategy to fabricate ultrathin $WO_3 \cdot H_2O$ nanosheets *via* ion etching and liquid-phase exfoliation of Aurivillius phase Bi_2WO_6. This strategy overcomes the previous issues of inadequate active sites within nanomaterials, yielding abundant ion transport channels to promote the electrochromic kinetics. Coupled with key reversible valence change and negligible structural strain of ultrathin nanosheets, the $WO_3 \cdot H_2O$ film demonstrates robust dual-band modulation in the visible–near-infrared wavelength range. In addition, a large-scale $WO_3 \cdot H_2O$ film (10 × 10 cm^2) can be fabricated using a stable spraying ink, which offers promising prospects for up-scalable production of smart windows. The outdoor test and the energy-saving simulation reveal that large-sized smart windows based on $WO_3 \cdot H_2O$ films not only achieve a significant indoor temperature modulation but also greatly reduce the energy consumption of the building, demonstrating their good thermal regulation and energy-saving capabilities. This work offers new insights into the structural design of nanomaterials *via* a top-down strategy, providing a promising route for fabricating other 2D electrochromic materials and highlighting the potential for application of smart windows in energy-saving buildings.

Introduction

Increasing global energy consumption has reinforced the pursuit of reliable and sustainable energy-saving techniques. Among them, electrochromic devices stand out as highly attractive for energy-saving smart windows and displays, owing to their reversible photothermal modulation ability and remarkable optical memory performance.[1–7] In particular, electrochromic smart windows can dynamically regulate indoor brightness and temperature, potentially reducing the energy consumption of buildings by up to 40%.[8] As a critical component of smart windows, tungsten trioxide (WO_3) has emerged as one of the most promising electrochromic materials for commercialization owing to its low cost and obvious color variation.[9] Its rich crystal structure provides a multidimensional design space for electrochromic smart windows.[10] In addition, WO_3 exhibits broad spectral modulation from visible–near-infrared (VIS-NIR) to mid-infrared regions.[11–14] The independent dual-band modulation of WO_3 in the VIS-NIR region endows smart windows with efficient photothermal modulation, consolidating its contribution to the

[a] Key Laboratory for Special Functional Materials of Ministry of Education, National & Local Joint Engineering Research Center for High-Efficiency Display and Lighting Technology, and School of Nanoscience and Materials Engineering, Henan University, Kaifeng 475004, China. E-mail: jinhui.wang@henu.edu.cn, caiguofa@henu.edu.cn

[b] Smart Materials for Architecture Research Lab, Innovation Center of Yangtze River Delta, Zhejiang University, Jiaxing, 314100, China. E-mail: yangguojian@zju.edu.cn

energy-saving of buildings.[15–17] Despite these remarkable advantages, the hysteresis issue associated with ion transport in WO_3 still needs to be effectively addressed.

To address this issue, substantial efforts have been devoted to constructing nanostructured WO_3 crystals to optimize the ion transport properties for improving electrochromic performance.[18,19] Among them, two-dimensional (2D) nanostructures are widely acknowledged in electrochromic applications because their large surface area can efficiently facilitate ion participation in redox reactions.[20] Moreover, 2D nanostructures adhere tightly to the substrate *via* abundant van der Waals forces, reducing the interfacial resistance to enable rapid electron transfer. Their interlaced and stacked networks evenly redistribute the strain of 2D nanostructures, improving the mechanical durability of electrodes.[21] In recent years, some efforts have been made to improve the electrochromic performance of WO_3 by constructing nanosheet structures.[22–26] Nanosheets with thicknesses of 20–50 nm can offer a large electrolyte contact area and reduced ion transport distance, thereby improving the electrochromic switching speed and optical modulation. Theoretically, reducing the thickness of the nanosheet structure can further increase the specific surface area and expose the active sites, preventing ion transport from being confined by interlayer interactions.[27] However, efficiently exposing active surfaces and optimizing ion accessibility in ultrathin architectures remain critical challenges. It becomes an urgent task to rationally design ultrathin nanosheet structures of WO_3, realizing the comprehensive improvement of its electrochromic properties.

Herein, we developed a facile top-down approach to efficiently fabricate ultrathin $WO_3{\cdot}H_2O$ nanosheets with an average thickness of 4.5 nm *via* ion etching of Aurivillius Bi_2WO_6 and liquid-phase exfoliation, which can produce abundant active sites to promote the electrochromic reaction. The ultrathin nanosheet structure with reversible valence changes and negligible structural strain endows the ultrathin $WO_3{\cdot}H_2O$ nanosheet film with excellent dual-band modulation in the VIS-NIR wavelength range, including large optical modulation (90% and 90.5% at 633 and 1200 nm, respectively), fast switching speed (<10 s), and excellent cycling stability of 5000 cycles (maintaining 80%). As a proof-of-concept, we constructed a self-powered smart window with a size of 10×10 cm^2 by establishing a potential gradient between a $WO_3{\cdot}H_2O$ electrode, an etched carbon paper (ECP) electrode, and an Al-based metal electrode. Compared with the bleaching state, the self-powered smart window in the colored state can achieve substantial temperature modulation of 12 °C in a model house. The simulation results demonstrate that buildings installed with self-powered smart windows can save energy up to 20.7% (168.8 MJ m^{-2}) in the energy consumption of heating, ventilation, and air conditioning (HVAC) systems in Sacramento. This top-down strategy for preparing ultrathin $WO_3{\cdot}H_2O$ provides a promising route for fabricating other 2D electrochromic materials, highlighting the potential of self-powered smart windows in energy-saving building applications.

Results and discussion

Preparation of ultrathin $WO_3{\cdot}H_2O$ nanosheets

Ultrathin $WO_3{\cdot}H_2O$ nanosheets were obtained by selectively etching $[Bi_2O_2]^{2+}$ layers in Aurivillius Bi_2WO_6 and surface tension-induced exfoliation (Fig. 1a and Experimental methods, SI). In detail, Aurivillius Bi_2WO_6 was fabricated *via* a hydrothermal method, in which an atomically stacked $[Bi_2O_2]^{2+}$ layer and $[WO_6]^{2-}$ layer share corner oxygens.[28] Upon acid etching the $[Bi_2O_2]^{2+}$ layer, H^+ reacts with $[WO_6]^{2-}$ to produce H_2O molecules, which occupy the interlayer space of WO_3 structures. X-ray diffraction (XRD) revealed the transformation of Bi_2WO_6 into $WO_3{\cdot}H_2O$ (Fig. 1b). The main crystalline phase of Bi_2WO_6 can be indexed to an anisotropic orthorhombic structure extending along the (113) and (200) directions (JCPDS# 73–2020). After the etching of Bi_2WO_6, the sample shows distinct diffraction peaks at 16.5°, 25.6°, and 35°, which correspond to the (020), (111) and (121) planes of well-ordered orthorhombic $WO_3{\cdot}H_2O$ (JCPDS# 84–886), respectively. In addition, the (111) diffraction peak of $WO_3{\cdot}H_2O$ shifts to a lower angle than that of the standard card, demonstrating an enlarged interlayer space after etching $[Bi_2O_2]^{2+}$.[29] Moreover, the thermogravimetric analysis (TGA) reveals that the sample exhibits 7.3% of weight loss between 100 and 400 °C, which can be attributed to the evaporation of structural water in $WO_3{\cdot}H_2O$. The calculated water content coincides with the XRD results, in which one WO_3 unit is combined with a structural water (Fig. S2, SI). The $WO_3{\cdot}H_2O$ obtained from Bi_2WO_6 exhibits a spherical nanostructure with stacked nanosheets. Therein, elemental mapping reveals that the obtained $WO_3{\cdot}H_2O$ only contains W and O elements, proving the successful etching of Bi element in Bi_2WO_6 (Fig. S3, SI). Furthermore, the chemical composition and valence state of $WO_3{\cdot}H_2O$ were characterized *via* X-ray photoelectron spectroscopy (XPS, Fig. S4, SI). The characteristic peaks of only W, O, and C demonstrate the purity of WO_3. The characteristic peaks of W $4f_{7/2}$, W $4f_{5/2}$, and W $5p_{3/2}$ are located at 35.7, 37.9, and 41.5 eV, respectively, in the W 4f spectrum, suggesting that W maintains the highest oxidation state of W^{6+}. Additionally, the characteristic peaks of W═O and H–O bonds are located at 530.5 and 532.4 eV in the O 1s spectrum, indicating the presence of structural water. The above results demonstrate that $WO_3{\cdot}H_2O$ was successfully prepared by etching Bi_2WO_6.

Ultrathin $WO_3{\cdot}H_2O$ nanosheets can be further obtained *via* the liquid-phase exfoliation of $WO_3{\cdot}H_2O$, the ultrathin nanosheet can enrich the active sites and reduce the ion diffusion distance.[24] The exfoliation efficiency of $WO_3{\cdot}H_2O$ can be optimized by matching the polarity and dispersive force ratio of mixed *N*,*N*-dimethylformamide (DMF)/H_2O solvents.[30,31] By adjusting the component ratios of DMF and H_2O, we found that the polarity/dispersive force ratio of the mixed solvent with 50% DMF is 1.15, which is closest to that of $WO_3{\cdot}H_2O$ (1.21) (Fig. S5 and the detailed discussion in Section S1, SI). In addition, the $WO_3{\cdot}H_2O$ dispersed in the mixed solvent with 50% DMF exhibited the deepest yellow-green color and minimal precipitation amount compared to the other mixed solvents. Both results confirm the highest exfoliation yield of $WO_3{\cdot}H_2O$ nanosheets in the mixed solvent with 50% DMF. Furthermore, the $WO_3{\cdot}H_2O$ obtained from 50% DMF is predominantly in the form of ultrathin nanosheets with smaller dimensions

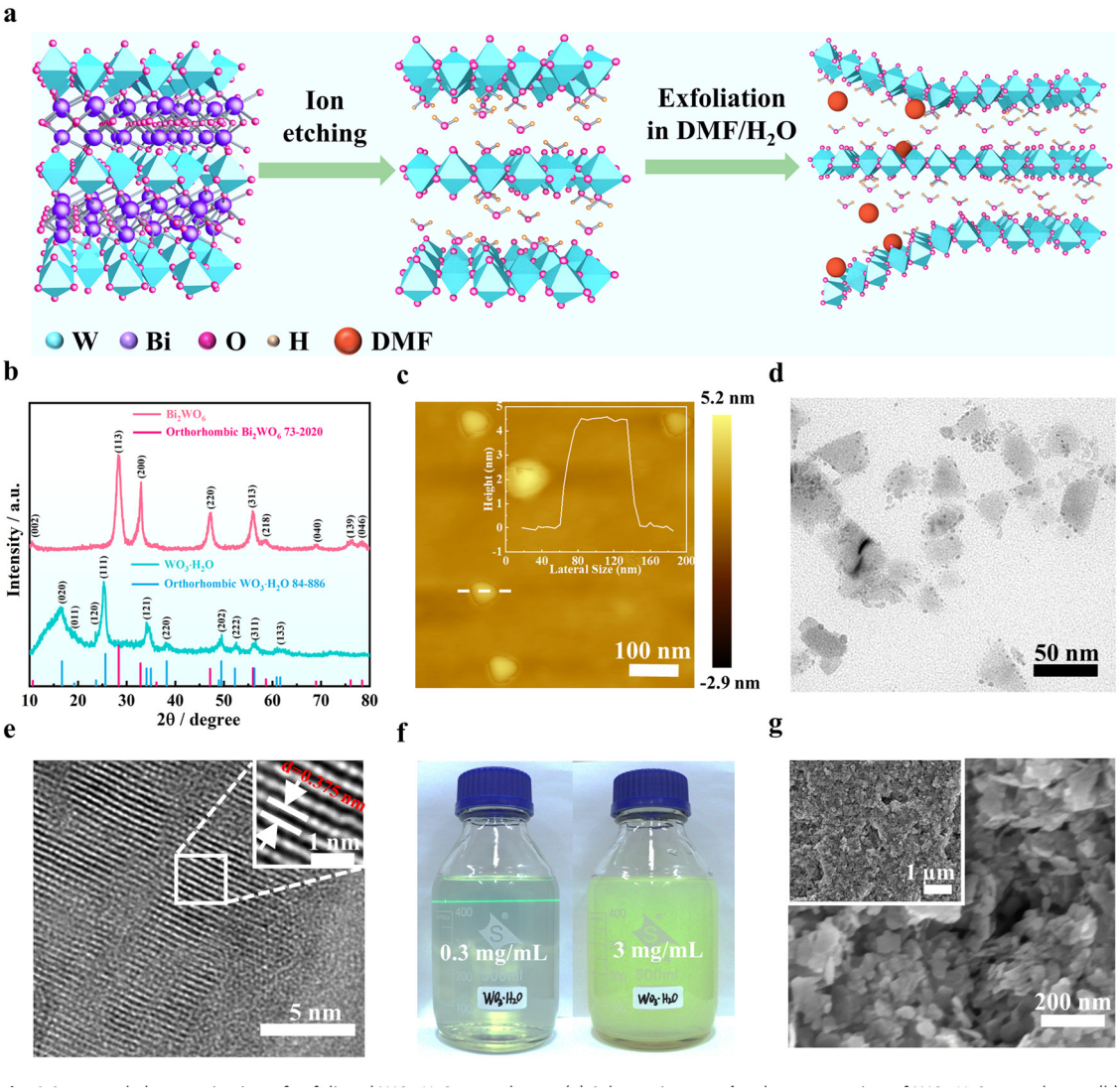

Fig. 1 Structural characterization of exfoliated $WO_3{\cdot}H_2O$ nanosheets. (a) Schematic route for the preparation of ultrathin $WO_3{\cdot}H_2O$ nanosheets. (b) XRD patterns of Bi_2WO_6 and $WO_3{\cdot}H_2O$. (c) AFM image and height profile of $WO_3{\cdot}H_2O$ nanosheets after liquid-phase exfoliation. (d) TEM and (e) lattice fringe images of $WO_3{\cdot}H_2O$ nanosheets. (f) Photograph of exfoliated $WO_3{\cdot}H_2O$ nanosheets in an ethanol/water (volume ratio of 1 : 1) solution. (g) SEM image of $WO_3{\cdot}H_2O$ nanosheet film.

than other mixed solvents (Fig. 1c and Fig. S6, SI). The corresponding random statistics for 100 samples demonstrate that 67% of the nanosheets show an average thickness of 4.5 nm and 76% with lateral dimensions less than 100 nm (Fig. S7, SI). When the amount of DMF is reduced to 10%, the average thickness of the $WO_3{\cdot}H_2O$ nanosheets increases to 7 nm, and only 60% of the nanosheets with lateral dimensions are less than 100 nm. Furthermore, transmission electron microscopy (TEM) reveals the low contrast of the exfoliated $WO_3{\cdot}H_2O$ nanosheets, confirming the ultrathin nanostructural nature of $WO_3{\cdot}H_2O$ (Fig. 1d). In addition, a small number of nanodots with sizes less than 10 nm were formed due to the shear stress effect during liquid-phase exfoliation. The clear lattice spacing of 3.75 Å corresponds to the (120) interplanar spacing (Fig. 1e), consistent with the XRD results. To fabricate electrochromic films, a homogeneous ink consisting of ultrathin $WO_3{\cdot}H_2O$ nanosheets was prepared with a mixed ethanol/water solvent (v/v = 1 : 1) (Fig. 1f). The pronounced Tyndall effect suggests good dispersibility of ultrathin $WO_3{\cdot}H_2O$ in the ink. By spraying the ink on the FTO substrate *via* facile spray coating, the porous ultrathin $WO_3{\cdot}H_2O$ film with a thickness of approximately 630 nm can be obtained (Fig. 1g and Fig. S8, SI). The nanosheets and porous structure can increase the contact area with the electrolyte and shorten the ion transport distance, thereby promoting more active sites to participate in the reaction.

Electrochromic performance of ultrathin $WO_3{\cdot}H_2O$ films

To verify the superiority of ultrathin nanosheets, the electrochemical and electrochromic performances of unexfoliated, multilayer, and ultrathin $WO_3{\cdot}H_2O$ films were evaluated in a three-electrode spectroelectrochemical cell. Cyclic voltammetry (CV) measurement of the films was carried out at a scan rate of 20 mV s^{-1} in a potential window of −0.7 to 0.5 V (*vs.* Ag^+/Ag),

and the transmittance change was recorded in real-time at a wavelength of 633 nm *via* a dynamic transmittance spectrum (Fig. 2a). During the cathodic polarization from 0.5 to −0.7 V (*vs.* Ag^+/Ag), the ultrathin $WO_3{\cdot}H_2O$ film experiences a reduction process from W^{6+} to W^{5+}. As the reduction potential gradually increases to −0.7 V (*vs.* Ag^+/Ag), the film color transitions from transparent to deep blue, and its transmittance decreases from 94% to 10%. During the anodic polarization from −0.7 to 0.5 V (*vs.* Ag^+/Ag), the CV curve exhibits a pronounced oxidation peak around −0.28 V (*vs.* Ag^+/Ag). As the oxidation potential gradually increases to 0.5 V (*vs.* Ag^+/Ag), the film gradually recovers to the initial transparent state with a transmittance of 94%. The electrochromic process of the $WO_3{\cdot}H_2O$ film can be expressed as follows:

$$WO_3{\cdot}H_2O + xH^+ + xe^- \leftrightarrow H_xWO_3{\cdot}H_2O \quad (1)$$

During the CV process, the closed dynamic transmittance spectrum demonstrates that the ultrathin $WO_3{\cdot}H_2O$ film can achieve efficient and reversible color variation. Moreover, the CV curves reveal that the ultrathin $WO_3{\cdot}H_2O$ film exhibits a larger response current density and lower oxidation potential than the unexfoliated and multilayer $WO_3{\cdot}H_2O$ films (Fig. S9, SI). This is mainly because ultrathin $WO_3{\cdot}H_2O$ nanosheets can efficiently expose more active sites to facilitate ion insertion/extraction.

The optical modulation is the transmittance difference of the film between the bleached and the colored state, which can reflect the ability of the film to modulate light and radiant heat. By applying a small cathodic potential of −0.2 V (*vs.* Ag^+/Ag), the ultrathin $WO_3{\cdot}H_2O$ film displays an optical modulation of 81% at 1200 nm (NIR region) while maintaining a high transmittance of 69% at 633 nm (VIS region, Fig. 2b). This finding indicates that the film can selectively block most of the NIR heat and achieve the "bright-cool" mode. This selective NIR modulation originates from the localized surface plasmon resonance effect on the surface of $WO_3{\cdot}H_2O$ owing to the ion adsorption/desorption process.[32] When the cathodic potential increased to −0.7 V (*vs.* Ag^+/Ag), the ultrathin $WO_3{\cdot}H_2O$ film displays an ultralow transmittance of approximately 0% at 1200 nm and approximately 4% at 633 nm, which is referred to as the "dark-cool" mode. Upon applying an opposite anodic potential of 0.5 V (*vs.* Ag^+/Ag), the ultrathin $WO_3{\cdot}H_2O$ film can return to the initial "bright" mode, showing high transmittance across the broad NIR–VIS region. In this case, the ultrathin $WO_3{\cdot}H_2O$ film achieves ultra-large optical modulations of 90% and 90.5% at 633 and 1200 nm, respectively, which are superior to those of most previously reported works (Table S3, SI).[1,12,33–38] Moreover, its optical modulations are also significantly higher than those of the unexfoliated and multilayer $WO_3{\cdot}H_2O$ films (Fig. S10, SI), owing to the large specific surface area and the highly active surface of ultrathin nanosheets. Solar radiation comprises 50% of the total energy distributed in the VIS region and 47% in the NIR region.[39] To assess the dynamic optical regulation of the film, the transmittance spectra in three modes are converted into solar irradiance spectra (Fig. 2c and Table S4, SI). In the "bright" mode, the film delivers high transmittance for solar irradiance, allowing

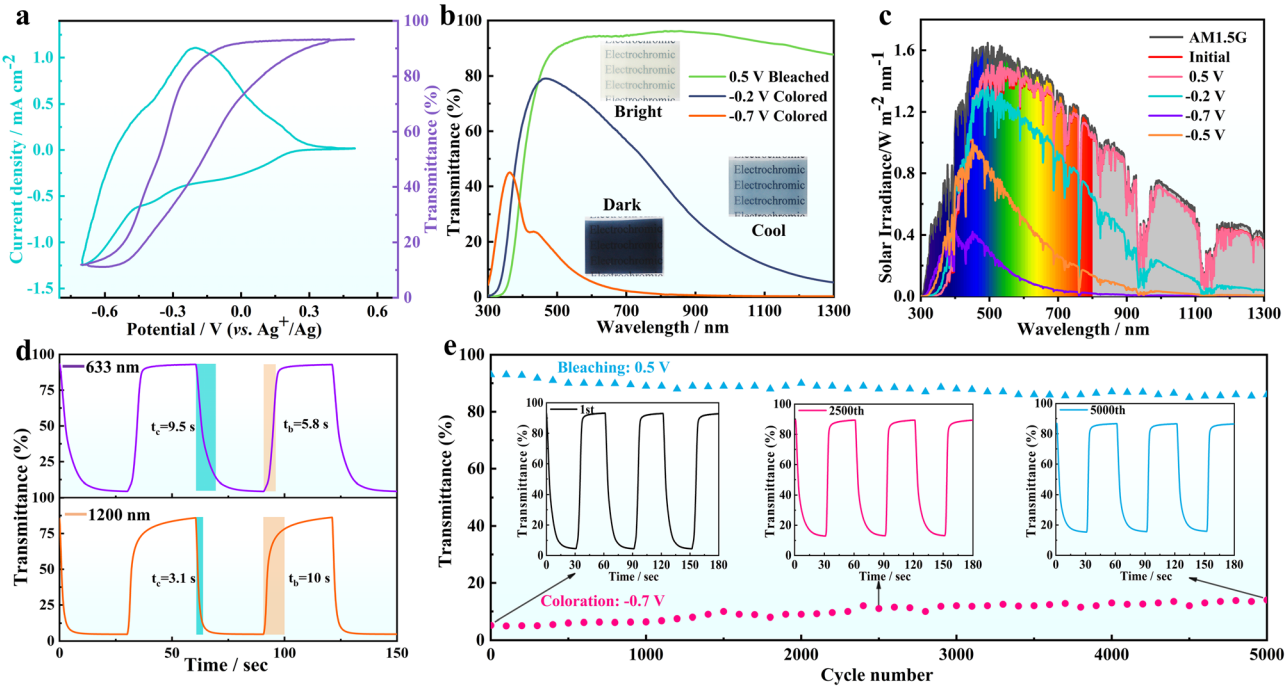

Fig. 2 Electrochromic and electrochemical performance of the ultrathin $WO_3{\cdot}H_2O$ film in 0.5 M H_2SO_4 electrolyte. (a) CV curve and *in situ* transmittance spectrum of the film at 633 nm at a scan rate of 20 mV s^{-1}. (b) Optical transmittance spectra and (c) Solar irradiance spectra of the film in three distinct modes in the range of 300–1300 nm. (d) Dynamic transmittance spectra of the film at 633 and 1200 nm under alternating potentials of 0.5/−0.7 V and 0.5/−0.2 V (*vs.* Ag^+/Ag). (e) Cycling performance of the film was tested at −0.7 and 0.5 V (*vs.* Ag^+/Ag) for 30 s at 633 nm.

94.8% of the NIR heat and 91.2% of the VIS light to pass. In the "bright-cool" mode, the film blocks 82.5% of the NIR heat while providing high VIS transmittance (75.5%). In the "dark-cool" mode, the film can block most of the VIS light (87.9%) and NIR heat (99.5%). Therefore, the ultrathin $WO_3{\cdot}H_2O$ film can deliver selective VIS–NIR regulation, providing the significant advantages of protecting personal privacy and reducing building energy consumption.

The switching speed refers to the time required to achieve 90% of the largest optical modulation of the electrochromic films, which is a crucial indicator for evaluating the electrochromic reaction kinetics.[40,41] We investigated the switching characteristics of ultrathin $WO_3{\cdot}H_2O$ films in the VIS–NIR region *via* a combination of dynamic transmittance spectra and potentiostatic methods (Fig. 2d). Upon application of periodic potentials of −0.7/0.5 V and −0.2/0.5 V (*vs.* Ag^+/Ag), the film exhibits switching times of 9.5/5.8 s and 3.1/10 s for coloration/bleaching at 633 and 1200 nm, respectively. The switching time is shorter than those of unexfoliated/multilayer $WO_3{\cdot}H_2O$ films and comparable to those of the most reported similar-size WO_3 samples (Fig. S11, SI).[42,43] The enhanced switching speed is due to the shortened ion diffusion distance from the ultrathin nanosheets. Furthermore, the long-term cycling stability of these films between the coloration and bleaching states was evaluated by alternately applying potentials of −0.7 and 0.5 V (*vs.* Ag^+/Ag) for 30 s. The ultrathin $WO_3{\cdot}H_2O$ film delivers an excellent optical modulation retention of 98% after 1000 cycles (Fig. S12, SI), which is much higher than that of the unexfoliated film (53%) and multilayer film (86%). Generally, the cyclic performance of WO_3 films in acidic electrolytes is typically limited to 3000 cycles. Notably, our ultrathin $WO_3{\cdot}H_2O$ film maintains 80% of its initial optical modulation even after 5000 cycles, outperforming most previously reported WO_3 films (Fig. 2e).[10,44,45] The remarkable cycling stability of the ultrathin $WO_3{\cdot}H_2O$ film is attributed to the open structure of the ultrathin nanosheet and the porous morphology, which can greatly relieve the stress change of the material in the electrochromic process. The coloration efficiency (CE) is defined as the optical density change (ΔOD) in response to the per unit charge (ΔQ) inserted into the electrochromic film. It can be expressed by the following formula:

$$\mathrm{CE} = \frac{\Delta(\mathrm{OD})}{\Delta Q} = \frac{\log(T_b/T_c)}{\Delta Q} \quad (2)$$

where T_b and T_c represent the transmittance of the film in the bleached and colored states, respectively. According to the slope of the linear region of the ΔOD variation under different current densities (Fig. S13, SI), the ultrathin $WO_3{\cdot}H_2O$ film

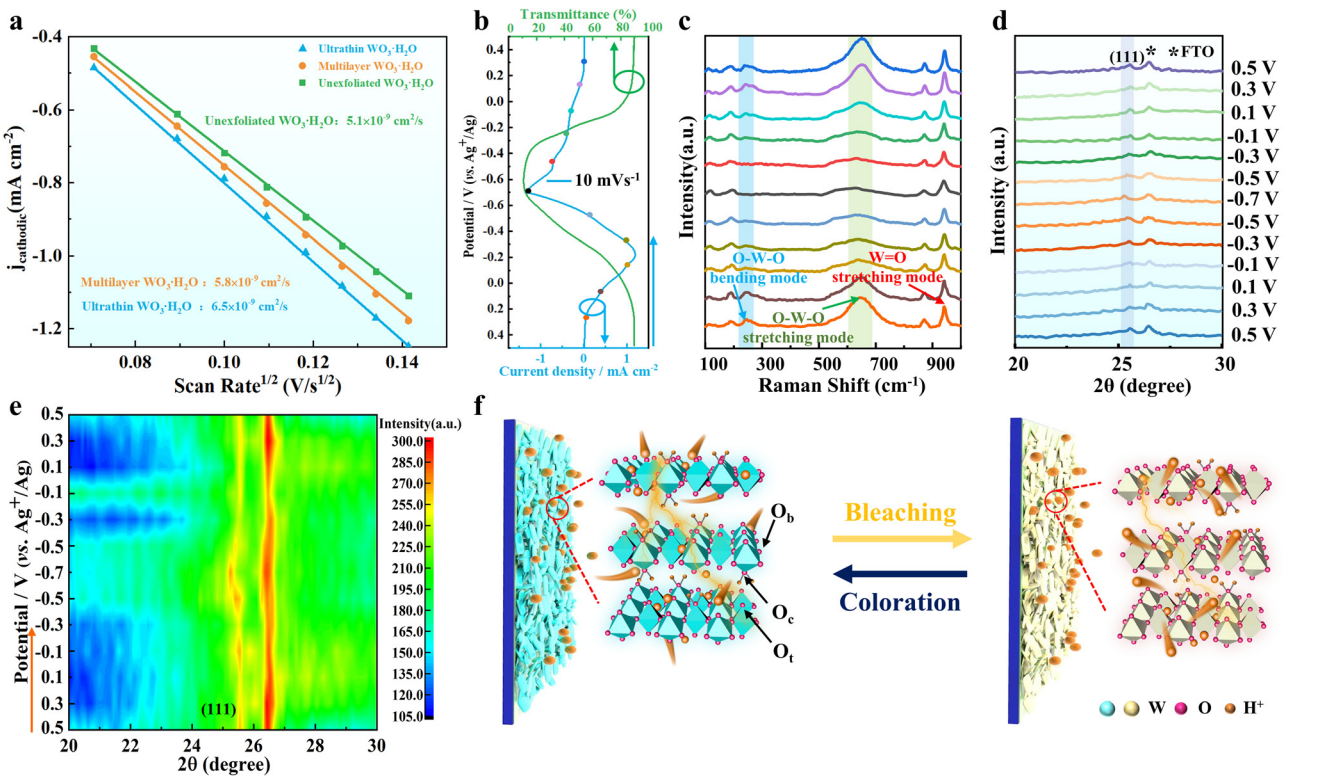

Fig. 3 Mechanism characterization of ultrathin $WO_3{\cdot}H_2O$ films during H^+ insertion/extraction. (a) Diffusion coefficient measurement of unexfoliated, multilayer and ultrathin $WO_3{\cdot}H_2O$ films using the cathodic peak current as a function of the square root of the scan rates. (b) CV curve at 10 mV s^{-1} in 0.5 M H_2SO_4 electrolyte and *in situ* transmittance spectrum at 633 nm of the ultrathin $WO_3{\cdot}H_2O$ film. (c) *In situ* Raman signal evolution of an ultrathin $WO_3{\cdot}H_2O$ film corresponding to the CV curve (b) at 10 mV s^{-1}. (d) *In situ* XRD patterns of ultrathin $WO_3{\cdot}H_2O$ films at 2θ values ranging from 20° to 30°. (e) Chromaticity diagram of ultrathin $WO_3{\cdot}H_2O$ films under different voltages. (f) Schematic of H^+ transportation in ultrathin $WO_3{\cdot}H_2O$ films during bleaching and coloration.

delivers CE values of 65 $cm^2\ C^{-1}$ at 633 nm and 199 $cm^2\ C^{-1}$ at 1200 nm, which are higher than those of the multilayer $WO_3 \cdot H_2O$ film (33 and 138 $cm^2\ C^{-1}$ at 633 and 1200 nm) and the unexfoliated $WO_3 \cdot H_2O$ film (28 and 70 $cm^2\ C^{-1}$ at 633 and 1200 nm).

Electrochromic mechanism of ultrathin $WO_3 \cdot H_2O$ nanosheets

To gain insight into the dynamics of ion transport, we sought to assess the H^+ diffusion coefficient D_0 ($cm^2\ s^{-1}$) within the ultrathin $WO_3 \cdot H_2O$ film *via* the Randles–Sevcik formula:[46]

$$i_p = (2.69 \times 10^5) n^{3/2} A D_0^{1/2} \nu^{1/2} C_0 \quad (3)$$

where i_p, n, A, $\nu^{1/2}$, and C_0 represent the peak current, the number of electrons (assumed to be 1), the active area of the electrode reaction (cm^2), the square root of the scan rate and the H^+ concentration (mol cm^{-3}), respectively. The D_0 values of the ultrathin $WO_3 \cdot H_2O$ film in the coloration and bleaching processes are 6.5×10^{-9} and 6×10^{-9} $cm^2\ s^{-1}$, respectively, which are much higher than those of previously reported WO_3 films (Fig. 3a and Fig. S14, SI).[21,47–50] Furthermore, the Nyquist plots reveal that the ultrathin $WO_3 \cdot H_2O$ films retain consistent charge transfer impedances with multilayer and unexfoliated films in the high-frequency region, but exhibit lower diffusion-controlled Warburg impedance in the low-frequency region (Fig. S15, SI). Moreover, we confirmed the role of structural water in the $WO_3 \cdot H_2O$ film by comparison with the anhydrous WO_3 film. According to the TGA curve, the anhydrous WO_3 film was obtained by subjecting the $WO_3 \cdot H_2O$ film to heat treatment at 250 °C. Without structural water, the WO_3 film delivers large optical modulation, but shows a significant decrease in the switching speed and cycling stability (Fig. S16, SI). These results confirm that the ultrathin nanosheets with structural water in the film can facilitate H^+ diffusion and stabilize the structure, resulting in fast color switching and high cycling stability.

To further understand the electrochromic mechanism of the ultrathin $WO_3 \cdot H_2O$ film, *in situ* Raman and dynamic transmittance spectra measurements were carried out during real-time CV measurements within a potential window of 0.5 to −0.7 V (*vs.* Ag^+/Ag) at 10 mV s^{-1} (Fig. 3b and c). In the coloration process, the Raman peaks at 243 cm^{-1} and 650 cm^{-1}, corresponding to the bending vibration and stretching vibration of O–W–O, gradually weaken until they disappear with cathodic polarization. This corresponds to the semiconductor-to-metal transition process of $WO_3 \cdot H_2O$ owing to the reduction of W^{6+} to W^{5+} with continuous H^+ insertion. In the bleaching process, both Raman peaks of the ultrathin $WO_3 \cdot H_2O$ film at 243 cm^{-1} and 650 cm^{-1} recover the initial intensity upon H^+ extraction, representing the valence state transition from W^{5+} to W^{6+} and a reversible metal–semiconductor switching in $WO_3 \cdot H_2O$. This result indicates the reversible valence change of the ultrathin $WO_3 \cdot H_2O$ film in the electrochromic process.

In situ XRD was further utilized to investigate the structural evolution of the ultrathin $WO_3 \cdot H_2O$ film during the electrochromic process (Fig. 3d and e). There is no obvious shift in most characteristic peaks of the ultrathin $WO_3 \cdot H_2O$ film during the electrochromic process other than the (111) peak (Fig. S17, SI). During the cathodic polarization from 0.5 V to −0.7 V (*vs.* Ag^+/Ag), the (111) diffraction peak gradually shifts from 25.53° to 25.33°, indicating that the lattice expands by only 0.02 Å with H^+ insertion (Fig. 3d). After applying the reverse anodic potential of 0.5 V (*vs.* Ag^+/Ag), the (111) peak of the ultrathin $WO_3 \cdot H_2O$ film can return to the initial position, demonstrating the highly reversible reaction of $WO_3 \cdot H_2O$. Chromaticity analysis summarizes the XRD peak intensity and position evolution (Fig. 3e). No diffraction peaks appeared or disappeared from the ultrathin $WO_3 \cdot H_2O$ film, indicating that $WO_3 \cdot H_2O$ undergoes a low-strain structure change without phase transition and hence features excellent structural stability during the electrochromic process.[29,51]

Based on the *in situ* measurements and electrochromic performance characterization, we sought to further elucidate the electrochromic process of ultrathin $WO_3 \cdot H_2O$ nanosheets (Fig. 3f). The active sites of ultrathin $WO_3 \cdot H_2O$ nanosheets in the electrochromic process are efficiently exposed by ion etching Aurivillius Bi_2WO_6 and liquid-phase exfoliation. In addition, the potential oxygen sites for H^+ binding in $WO_3 \cdot H_2O$ can be divided into bridging oxygen (O_b), terminal oxygen (O_t), and coordinated oxygen (O_c).[52] Under a small voltage, some protons are preferentially bind to O_b by adsorption, while other protons are embedded inside $WO_3 \cdot H_2O$ and bind to O_t when the voltage increases.[29] In this case, the electrochromic performance of the ultrathin $WO_3 \cdot H_2O$ film is determined by three potential oxygen sites for H^+ binding: O_b, O_t, and O_c. The NIR regulation of the ultrathin $WO_3 \cdot H_2O$ film is due to H^+ adsorption/desorption, which is highly associated with the O_b site on the $WO_3 \cdot H_2O$ surface. Then the H^+ accesses the interior crystal cavity and binds to the O_t site, causing a redox reaction and VIS light absorption. Nevertheless, H^+ is unlikely to combine with the O_c site because of the repulsive effect of the coordinated water.

Electrochromic energy storage properties of ultrathin $WO_3 \cdot H_2O$ nanosheets

Considering that both electrochromic and energy storage processes rely on redox reactions, the CV curves also indicate that the ultrathin $WO_3 \cdot H_2O$ film exhibits good energy storage capacity. Thus, we can integrate electrochromic and energy storage functions into a single system for multifunctional device exploitation. To demonstrate the feasibility of this concept, we measured the galvanostatic charge–discharge (GCD) and corresponding transmittance spectra of ultrathin $WO_3 \cdot H_2O$ films under different current densities (Fig. S18, SI). In the GCD experiments, the specific areal capacities of the ultrathin $WO_3 \cdot H_2O$ film are 19.6, 18.2, 17.9, 17.7, 16.6 and 16 μAh cm^{-2} under current densities of 0.1, 0.15, 0.25, 0.3, 0.4 and 0.6 mA cm^{-2}, respectively (Fig. S18a, SI). In addition, the symmetric shape of the GCD curve indicates the high Coulombic efficiency and electrochemical reversibility of the ultrathin $WO_3 \cdot H_2O$ film. In addition, real-time transmittance spectra during the GCD process were detected at a single wavelength of 633 nm to visualize energy storage (Fig. S18b, c, SI). Under galvanostatic current densities of 0.1 mA cm^{-2} and 0.6 mA cm^{-2}, the ultrathin $WO_3 \cdot H_2O$ film can achieve almost the same optical modulation in the charging process as the constant voltage charging potential of −0.7 V (*vs.* Ag^+/Ag). During the discharging process, this film can completely return to the transparent bleached state. This attractive visualization capability of the film could promote the potential application of

electrochromic-based energy storage indicators. The IR drop existing in the discharging curve is ascribed to the internal resistance of the film when a high current passes the film, causing the actual discharge voltage of the film to be lower than the charge voltage. In addition, the optical modulation of the ultrathin $WO_3{\cdot}H_2O$ film remains almost unchanged as the current density increases from 0.1 to 0.6 mA cm^{-2} during the GCD process (Fig. S18d, SI), illustrating the good rate capability of the film due to its rapid ion diffusion kinetics and robust electrochemical reversibility.

Performance evaluation of self-powered electrochromic devices

The electrochromic device (ECD) without external electrical supplies has attracted extensive attention in practical energy-saving applications such as smart windows. Here, we assembled a self-powered ECD using an ultrathin $WO_3{\cdot}H_2O$ film as the electrochromic electrode, Al foil as the negative electrode, and ECP as the positive electrode (Fig. 4a). Owing to the standard electrode potential of Al/Al^{3+} (*vs.* standard hydrogen electrode (SHE) being −1.66 V) being lower than that of the ultrathin $WO_3{\cdot}H_2O$ electrode, the potential difference between Al and the $WO_3{\cdot}H_2O$ electrode could drive H^+ insertion into the $WO_3{\cdot}H_2O$ electrode, resulting in the self-coloration of $WO_3{\cdot}H_2O$ (Fig. 4b). Moreover, the ECP results in a higher standard electrode potential (0.699 V *vs.* SHE) than the colored $WO_3{\cdot}H_2O$ (0.3 V *vs.* SHE). When the ECP and $WO_3{\cdot}H_2O$ electrodes were connected, extracting H^+ from $WO_3{\cdot}H_2O$ could result in self-bleaching of $WO_3{\cdot}H_2O$.[50,53] On the basis of this self-coloration mechanism, the ECD exhibits an optical modulation of 70% at 633 nm by connecting the $WO_3{\cdot}H_2O$ and Al electrodes for 700 s (the device as the baseline, Fig. 4c). When $WO_3{\cdot}H_2O$

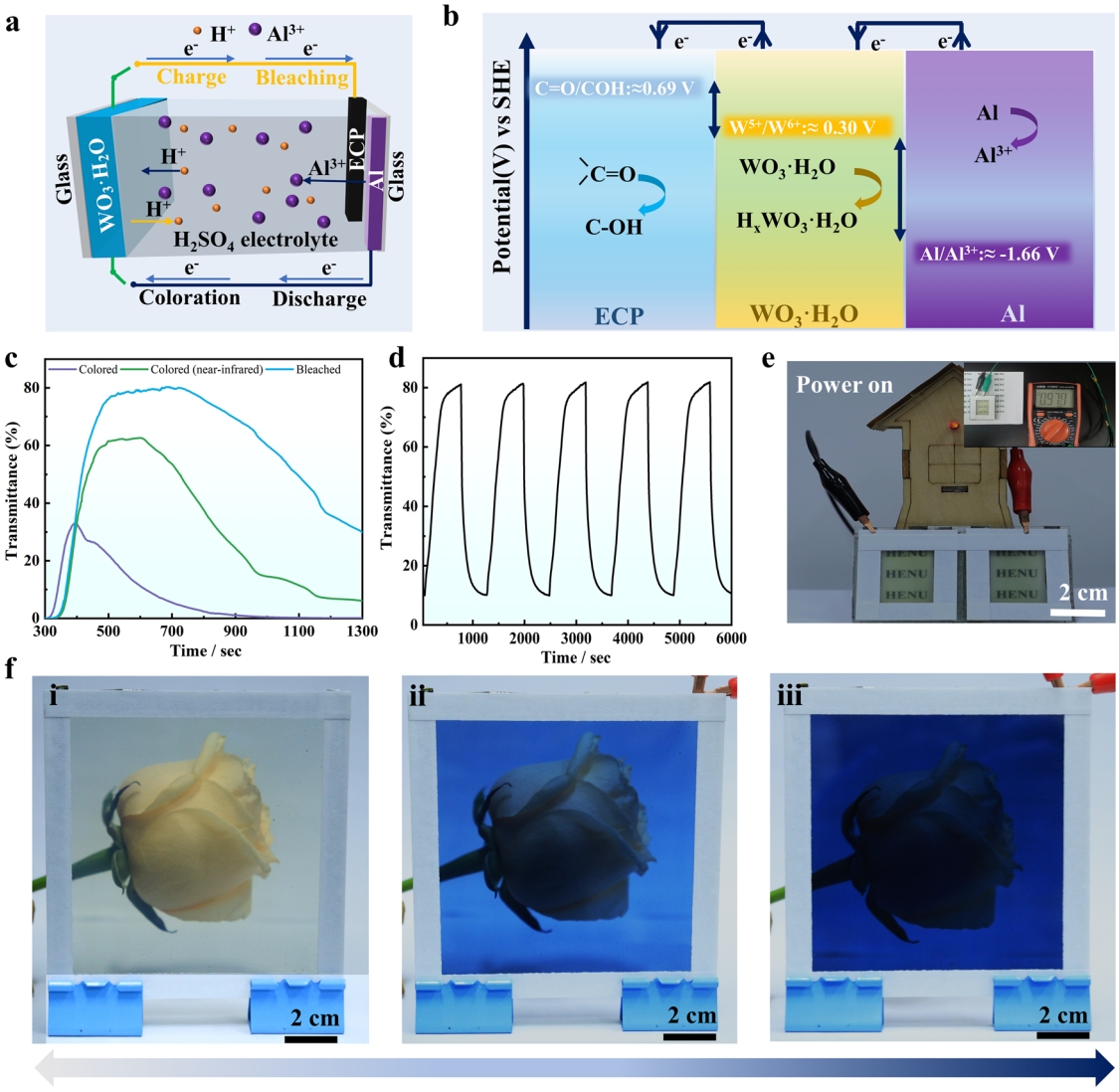

Fig. 4 Working mechanism and electrochromic performance of the self-powered ECD based on $WO_3{\cdot}H_2O$. (a) Schematic of the self-powered process and architecture of the ECD, including the $WO_3{\cdot}H_2O$ electrode connected with the Al/ECP electrode. (b) Energy level transition diagram of ECP, $WO_3{\cdot}H_2O$, and Al. (c) Optical transmittance spectra of the ECD after self-coloration for 30 and 500 s and self-bleaching for 700 s. (d) *In situ* dynamic transmittance spectra of the ECD. (e) An LED (1.5 V) driven by two ECD demos in series. (f) Digital photos of the ECD with a size of 10 × 10 cm^2 at different coloration times.

was connected to the ECP electrode, the ECD returned to its initial state after 500 s of self-bleaching. In addition, the self-coloration and self-bleaching time of the ECD are 151 and 331 s, respectively (Fig. 4d). Moreover, the ECD can maintain a stable cycle of 200 cycles in self-coloration and self-bleaching cycling tests (Fig. S19, SI). In addition, two ECDs (2.5 × 2 cm^2) in parallel can light up the LED for 40 minutes, indicating good energy storage performance of the ECD (Fig. 4e and Movie SI). Furthermore, we assembled a large-sized ECD (10 × 10 cm^2) to demonstrate its potential application as a smart window in buildings. Large-sized $WO_3 \cdot H_2O$ films were first successfully obtained by spray coating (Fig. S20, SI). The transmittance spectra confirm that the large-sized $WO_3 \cdot H_2O$ film presents nearly identical transmittance in five different areas, demonstrating its excellent film uniformity. The digital photos reveal that the large-sized ECD could still display high transmittance in the initial state, and dark blue color that obscured the flower background in the self-coloration state (Fig. 4f). The optical memory of ECD was further measured in an open-circuit state after applying 500 s of self-coloration. The dynamic spectrum reveals that the transmittance of the ECD decays by 18% within 1100 s (Fig. S21, SI). Therefore, the self-powered ECD proves good optical modulation and moderate memory properties, making it promising for smart windows that simultaneously protect indoor personal privacy and control indoor temperature to reduce energy consumption.

Application evaluation of the self-powered ECD as a smart window

To demonstrate the real-world applications of self-powered ECD in smart windows, we conducted a conceptual design and evaluated the indoor thermal regulation of a self-built model house equipped with ECD (Fig. 5a, b and Table S5, SI). A solar radiation lamp with a power of 300 W was used to simulate the sunlight for illumination. Prior to activating the solar radiation lamps, the indoor temperature of the model house was initialized at 22.5 °C. Upon switching the ECD to the "bright" mode, the indoor temperature of the model house under solar illumination swiftly rose to 34 °C within 10 minutes and gradually increased to 38 °C over the following 30 minutes. The high transmittance of the ECD in the VIS-NIR region ensures that most of the radiative heat enters the house. Conversely, when the ECD was switched to "bright-cool" and "dark-cool" modes, the indoor temperatures of the model house reached 28 °C and 26 °C under the same solar illumination, respectively. Compared with the "bright" mode, the ECD in the "bright-cool" and "dark-cool" modes can effectively reduce the indoor temperature of the model house by 10 °C

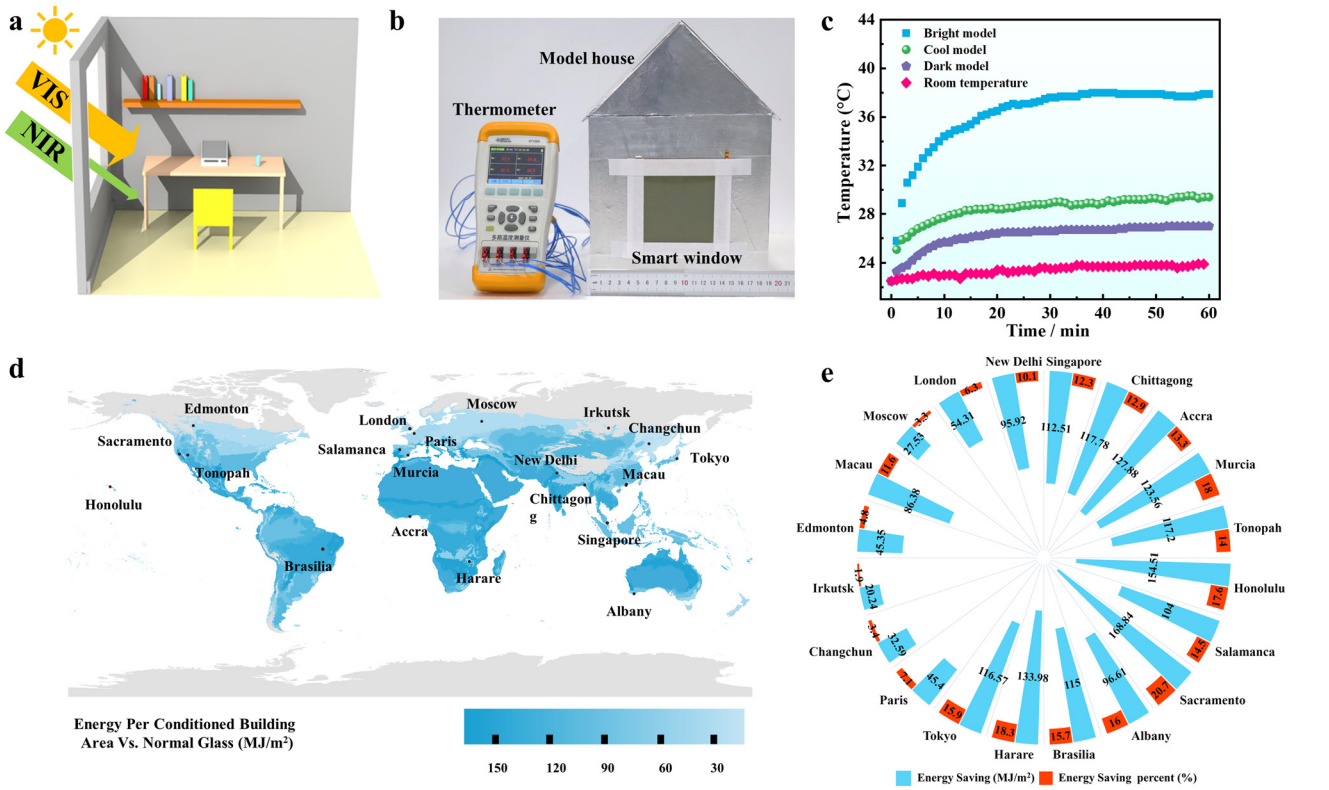

Fig. 5 Thermal regulation and energy-saving performance of the self-powered ECD. (a) Conceptual design of ECD in bright–cool model. (b) Digital photograph of a self-built model house with a temperature detector. (c) Indoor temperature changes in the model house when the self-powered smart window was used. (d) Simulative energy-saving performance of self-powered smart windows by region in estimated worldwide HVAC systems, with a commercial glass window as the baseline. (e) Annual energy savings and savings percentages for buildings with smart windows installed in typical cities.

and 12 °C, demonstrating their superior thermal regulation and energy-saving capabilities (Fig. 5c). To further evaluate the energy-saving performance of smart windows in different climate zones around the world, we conducted HVAC energy-saving simulations on an office building model ($30 \times 12 \times 9$ m^3) equipped with smart windows and further created a world map of energy-saving based on the Köppen–Geiger climate zone (Fig. 5d and Fig. S22 and Table S6, SI).[54,55] The HVAC energy-saving map of the world demonstrates that smart windows exhibit high energy-saving effects in temperate and tropical regions, particularly in Sacramento and Harare (Fig. 5e and Table S7, SI). In these two cities, buildings installed with smart windows demonstrate energy savings of 20.7% (168.8 MJ m^{-2}) and 18.3% (133.98 MJ m^{-2}) in HVAC energy consumption compared with standard buildings with traditional glass windows. Even in cold regions such as Moscow and Irkutsk, buildings with smart windows can achieve energy savings of 3.3% (27.5 MJ m^{-2}) and 1.9% (20.24 MJ m^{-2}), respectively. These findings indicate that our smart windows can significantly reduce HVAC energy usage in buildings located in hot regions, resulting in considerable energy-saving benefits and promising widespread application potential.

Conclusions

In summary, we fabricated ultrathin $WO_3{\cdot}H_2O$ films for electrochromic smart windows *via* ion etching of Aurivillius B_2WO_6 coupled with liquid-phase exfoliation. The ultrathin nanosheets feature $WO_3{\cdot}H_2O$ with a large surface area and efficient ion transport. As a result, the ultrathin $WO_3{\cdot}H_2O$ film exhibits significant dual-band regulation in the VIS–NIR region, realizing ultra-large optical modulations of 90% and 90.5% at 633 and 1200 nm, respectively, and fast switching speeds (9.5 and 3.1 s for coloration and 5.8 and 10 s for bleaching at 633 and 1200 nm, respectively). Moreover, the low-strain nature of the ultrathin $WO_3{\cdot}H_2O$ nanosheet structure endows the film with excellent cycling stability of 80% over 5000 cycles. On the basis of the potential gradient strategy, we further constructed self-powered large-scale ECDs using $WO_3{\cdot}H_2O$, ECP and Al electrodes, which possessed self-coloration and self-bleaching functions without an external electric supply. Both real-time temperature measurements and simulation calculations verifies that the ECD could achieve a thermal regulation of 12 °C in the model house and efficient HVAC energy savings in buildings. Our top-down strategy of ion etching and liquid-phase exfoliation offers insight into the fabrication of high-performance ultrathin nanosheet electrochromic materials, which show promising applications in energy-saving smart windows, self-supplied displays, smart power supplies, *etc.*

Author contributions

S. J. contributed to data curation, methodology and writing – original draft; S. J., X. G., Y. L., H. Z., G. Y., J. W. and G. C. contributed to the investigation, writing – review & editing; S. J. and J. W. contributed to the formal analysis and validation; J. W. and G. C. contributed to the conceptualization, funding acquisition, resources and supervision.

Conflicts of interest

There are no conflicts to declare.

Data availability

All data needed to support the conclusions in this work are present in the paper and the SI. Supplementary information: The supplemental information file contains experimental details, electrochemical measurement and calculation of the surface tension component ratio. In addition, supplemental data results such as TGA, SEM, XRD and XPS are included. See DOI: **https://doi.org/10.1039/d5mh01354b**.

Additional data related to this paper may be obtained upon request from the corresponding authors.

Acknowledgements

This work was supported by grants from the National Natural Science Foundation of China (Grant No. 62222402 and No. 52302361), the Program for Innovative Research Team (in Science and Technology) in the University of Henan Province (25IRTSTHN016), the Henan Natural Science Foundation (Grant No. 242300421213), and the Chinese Postdoctoral Science Foundation (Grant No. 2022M711036).

Notes and references

1 A. Llordes, G. Garcia, J. Gazquez and D. J. Milliron, *Nature*, 2013, **500**, 323–326.
2 C. Hu, X. Guo, Y. Gao, P. Zhang, P. Lei, Y. Lv, X. Wang, R. Zhu and G. Cai, *Mater. Horiz.*, 2025, **12**, 1962–1970.
3 J. Wang, X. Guo, C. Bian, Y. Zhong, J. Tu, P. S. Lee and G. Cai, *Prog. Mater. Sci.*, 2025, **153**, 101461.
4 G. Cai, X. Cheng, M. Layani, A. W. M. Tan, S. Li, A. L.-S. Eh, D. Gao, S. Magdassi and P. S. Lee, *Nano Energy*, 2018, **49**, 147–154.
5 Y. Zhou, Y. Lv, X. Guo, X. Wang, Z. Liu, J. Wang, Q. Sui, J. Wang, Z. Zeng and G. Cai, *Adv. Mater.*, 2025, e2502706.
6 Y. Huang, S. Wu, S. Zhao, Z. Guo, Z. Zhao, X. Wu, B. Wang, F. Wang, A. Xi, F. Lan, Y. Li, J. Xu, R. Li, Y. Zhao and R. Zhang, *Energy Environ. Sci.*, 2025, **18**, 1824–1834.
7 F. Zhao, C. Li, S. Li, B. Wang, B. Huang, K. Hu, L. Liu, W. W. Yu and H. Li, *Adv. Mater.*, 2024, **36**, 2405035.
8 L. Zhang, D. Chao, P. Yang, L. Weber, J. Li, T. Kraus and H. J. Fan, *Adv. Energy Mater.*, 2020, **10**, 2000142.
9 S. Cong, Y. Tian, Q. Li, Z. Zhao and F. Geng, *Adv. Mater.*, 2014, **26**, 4260–4267.
10 X. Tong, J. Wang, P. Zhang, P. Lei, Y. Gao, R. Ren, S. Zhang, R. Zhu and G. Cai, *Chem. Eng. J.*, 2023, **470**, 144130.

11 R. Giannuzzi, R. Scarfiello, T. Sibillano, C. Nobile, V. Grillo, C. Giannini, P. D. Cozzoli and M. Manca, *Nano Energy*, 2017, **41**, 634–645.
12 H. Gu, C. Guo, S. Zhang, L. Bi, T. Li, T. Sun and S. Liu, *ACS Nano*, 2018, **12**, 559–567.
13 P. Liu, B. Wang, C. Wang, L. Ma, W. Zhang, E. Hopmann, L. Liu, A. Y. Elezzabi and H. Li, *Adv. Funct. Mater.*, 2024, **34**, 2400760.
14 E. B. Franke, C. L. Trimble, M. Schubert, J. A. Woollam and J. S. Hale, *Appl. Phys. Lett.*, 2000, **77**, 930–932.
15 Y. Zhai, J. Li, S. Shen, Z. Zhu, S. Mao, X. Xiao, C. Zhu, J. Tang, X. Lu and J. Chen, *Adv. Funct. Mater.*, 2022, **32**, 2109848.
16 B. H. J. Zhong, J. X. Song, X. L. Zhang, L. Y. Du, Y. F. Gao, W. Liu and L. T. Kang, *Chem. Eng. J.*, 2024, **480**, 148098.
17 J. Wang, Z. Wang, L. Cui, M. Zhang, X. Huo and M. Guo, *Adv. Mater.*, 2024, **36**, 2406939.
18 T. Rao, Y. Zhou, J. Jiang, P. Yang and W. Liao, *Nano Energy*, 2022, **100**, 107479.
19 J. Liu, J. Zheng, J. Wang, J. Xu, H. Liu and S. Yu, *Nano Lett.*, 2013, **13**, 3589–3593.
20 L. Peng, P. Xiong, L. Ma, Y. Yuan, Y. Zhu, D. Chen, X. Luo, J. Lu, K. Amine and G. Yu, *Nat. Commun.*, 2017, **8**, 15139.
21 R. Li, X. Ma, J. Li, J. Cao, H. Gao, T. Li, X. Zhang, L. Wang, Q. Zhang, G. Wang, C. Hou, Y. Li, T. Palacios, Y. Lin, H. Wang and X. Ling, *Nat. Commun.*, 2021, **12**, 1587.
22 M. Dadkhah, M. J. Nine, K. Purasinhala, G. S. Sandhu and D. Losic, *Nano Mater. Sci.*, 2024, **12**, 2589.
23 J. Besnardiere, B. Ma, A. Torres-Pardo, G. Wallez, H. Kabbour, J. M. Gonzalez-Calbet, H. J. Von Bardeleben, B. Fleury, V. Buissette, C. Sanchez, T. Le Mercier, S. Cassaignon and D. Portehault, *Nat. Commun.*, 2019, **10**, 327.
24 P. T. G. Gayathri, S. S. Shaiju, R. Remya and D. Biswapriya, *Mater. Today Energy*, 2018, **10**, 380–387.
25 Z. Bi, X. Li, Y. Chen, X. He, X. Xu and X. Gao, *ACS Appl. Mater. Interfaces*, 2017, **9**, 29872–29880.
26 Z. Wang, W. Gong, X. Wang, Z. Chen, X. Chen, J. Chen, H. Sun, G. Song, S. Cong, F. Geng and Z. Zhao, *ACS Appl. Mater. Interfaces*, 2020, **12**, 33917–33925.
27 Y. Ma, N. Liu, L. Li, X. Hu, Z. Zou, J. Wang, S. Luo and Y. Gao, *Nat. Commun.*, 2017, **8**, 1207.
28 H. Ohkawa, M. Kudo, W. Sugimoto, N. Kumada, Z. Liu, O. Terasaki and Y. Sugahara, *Inorg. Chem.*, 2003, **42**, 4479–4484.
29 D. Wang, T. Xu, M. Zhang, Z. Ren, H. Tong and L. Shen, *Adv. Funct. Mater.*, 2023, **33**, 2211491.
30 J. Shen, J. Wu, M. Wang, P. Dong, J. Xu, X. Li, X. Zhang, J. Yuan, X. Wang, M. Ye, R. Vajtai, J. Lou and P. M. Ajayan, *Small*, 2016, **12**, 2741–2749.
31 D. K. Owens, *J. Appl. Polym. Sci.*, 2003, **14**, 1725–1730.
32 S. Zhang, S. Cao, T. Zhang and J. Lee, *Adv. Mater.*, 2020, **32**, 2004686.
33 A. Llordes, Y. Wang, A. Fernandez-Martinez, P. Xiao, T. Lee, A. Poulain, O. Zandi, C. A. Saez Cabezas, G. Henkelman and D. J. Milliron, *Nat. Mater.*, 2016, **15**, 1267–1273.
34 H. Sungyeon, K. Jongwook, K. O. Gary and J. M. Delia, *Nano Lett.*, 2017, **17**, 5756–5761.
35 K. Jongwook, K. O. Gary, W. Yang, L. Gabriel, E. W. Teresa, M. M. Tracy, A. H. Brett and J. M. Delia, *Nano Lett.*, 2015, **15**, 5574–5579.
36 Z. Wang, Q. Zhang, S. Cong, Z. Chen, J. Zhao, M. Yang, Z. Zheng, S. Zeng, X. Yang, F. Geng and Z. Zhao, *Adv. Opt. Mater.*, 2017, **5**, 1700194.
37 C. J. Dahlman, Y. Tan, M. A. Marcus and D. J. Milliron, *J. Am. Chem. Soc.*, 2015, **137**, 9160–9166.
38 M. Barawi, L. De Trizio, R. Giannuzzi, G. Veramonti, L. Manna and M. Manca, *ACS Nano*, 2017, **11**, 3576–3584.
39 A. Ghosh and T. K. Mallick, *Sol. Energy Mater. Sol. Cells*, 2018, **176**, 391–396.
40 Y. Yao, Q. Zhao, W. Wei, Z. Chen, Y. Zhu, P. Zhang, Z. Zhang and Y. Gao, *Nano Energy*, 2020, **68**, 104350.
41 G. Cai, J. Chen, J. Xiong, A. Lee-Sie Eh, J. Wang, M. Higuchi and P. S. Lee, *ACS Energy Lett.*, 2020, **5**, 1159–1166.
42 S. Zhang, S. Cao, T. Zhang, Q. Yao, A. Fisher and J. Y. Lee, *Mater. Horiz.*, 2018, **5**, 291–297.
43 S. Zhang, S. Cao, T. Zhang, A. Fisher and J. Y. Lee, *Energy Environ. Sci.*, 2018, **11**, 2884–2892.
44 G. Cai, M. Cui, V. Kumar, P. Darmawan, J. Wang, X. Wang, A. Lee-Sie Eh, K. Qian and P. S. Lee, *Chem. Sci.*, 2016, **7**, 1373–1382.
45 W. Q. Wang, X. L. Wang, X. H. Xia, Z. J. Yao, Y. Zhong and J. P. Tu, *Nanoscale*, 2018, **10**, 8162–8169.
46 V. Gau, S. C. Ma, H. Wang, J. Tsukuda, J. Kibler and D. A. Haake, *Methods*, 2005, **37**, 73–83.
47 M. Tian, R. Zheng and C. Jia, *Adv. Mater.*, 2024, **37**, 2409790.
48 M. Hassan, A. Ghaffar, G. Lou, Z. Miao, Z. Peng and K. Celebi, *Adv. Funct. Mater.*, 2024, **34**, 2310535.
49 M. Chen, J. Deng, H. Zhang, X. Zhang, D. Yan, G. Yao, L. Hu, S. Sun, J. Zhao and Y. Li, *Adv. Funct. Mater.*, 2024, **35**, 2413659.
50 W. Zhang, H. Li and A. Y. Elezzabi, *Adv. Funct. Mater.*, 2023, **33**, 2300155.
51 Z. Chen, Y. Peng, F. Liu, Z. Le, J. Zhu, G. Shen, D. Zhang, M. Wen, S. Xiao, C. P. Liu, Y. Lu and H. Li, *Nano Lett.*, 2015, **15**, 6802–6808.
52 R. Wang, Y. Sun, A. Brady, S. Fleischmann, T. B. Eldred, W. Gao, H. W. Wang, D. E. Jiang and V. Augustyn, *Adv. Energy Mater.*, 2020, **11**, 2003335.
53 Y. Luo, H. Jin, Y. Lu, Z. Zhu, S. Dai, L. Huang, X. Zhuang, K. Liu and L. Huang, *ACS Energy Lett.*, 2022, **7**, 1880.
54 H. E. Beck, N. E. Zimmermann, T. R. McVicar, N. Vergopolan, A. Berg and E. F. Wood, *Sci. Data*, 2018, **5**, 180214.
55 A. Shi, G. Yang, A. Ghani, Q. Lu, W. Ye, C. Mu, T. Jiang, Z. Pang, Y. Lu and G. Tan, *Chem. Eng. J.*, 2025, **509**, 161406.

